ACS NANO

www.acsnano.org

Strongly Quantum-Confined Perovskite Nanowire Arrays for Color-Tunable Blue-Light-Emitting Diodes

Yu Fu, Swapnadeep Poddar, Beitao Ren, Ying Xie, Qianpeng Zhang, Daquan Zhang, Bryan Cao, Yunqi Tang, Yucheng Ding, Xiao Qiu, Lei Shu, Jin-Feng Liao, Dai-Bin Kuang, and Zhiyong Fan*

Cite This: https://doi.org/10.1021/acsnano.2c02795 Read Online

ACCESS | Metrics & More | Article Recommendations | Supporting Information

ABSTRACT: **Color tunability of perovskite light-emitting diodes (PeLEDs) by mixed halide compositional engineering is one of the primary intriguing characteristics of PeLEDs. However, mixed halide PeLEDs are often susceptible to color red-shifting caused by halide ion segregation. In this work, strongly quantum-confined perovskite nanowires (QPNWs) made of $CsPbBr_3$ are grown in nanoporous anodic alumina templates using a closed space sublimation process. By tuning the pore size with atomic layer deposition, QPNWs with a diameter of 6.6 to 2.8 nm have been successfully obtained, with continuous tunable photoluminescence emission color from green (512 nm) to pure blue (467 nm). To better understand the photophysics of QPNWs, carrier dynamics and the benefit of alumina passivation are studied and discussed in detail. Eventually, PeLEDs using various diameters of $CsPbBr_3$ QPNWs are successfully fabricated with cyan color (492 nm) PeLEDs, achieving a record high 7.1% external quantum efficiency (EQE) for all $CsPbBr_3$-based cyan color PeLEDs. Sky blue (481 nm) and pure blue (467 nm) PeLEDs have also been successfully demonstrated, respectively. The work here demonstrates a different approach to achieve quantum-confined one-dimensional perovskite structures and color-tunable PeLEDs, particularly blue PeLEDs.**

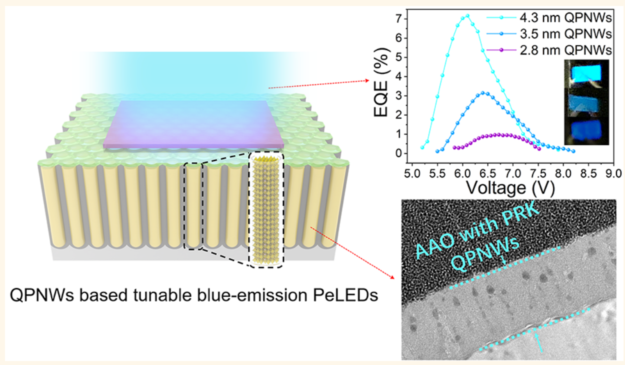

QPNWs based tunable blue-emission PeLEDs

KEYWORDS: *quantum confinement, perovskite, nanowires, anodized alumina, atomic layer deposition, blue emission LEDs*

INTRODUCTION

Metal halide perovskites have emerged as propitious candidates for perovskite light-emitting diodes (PeLEDs) due to high color purity,[1] tunable bandgap,[2] high photoluminescence quantum yields (PLQYs),[3] long charge diffusion lengths,[4] and desirably high defect tolerance.[5] In principle, the device emission color can be finely tuned by maneuvering the halide compositions, *i.e.*, I, Br, Cl, or mixed in specific ratios.[6−8] However, color instability stemming from halide ion-migration and segregation in mixed halides hinders further development of PeLEDs, especially the blue PeLEDs which require much higher turn on voltages.[9−13] Another viable approach to achieve color tunability of PeLEDs is to utilize quantum-confined perovskite nanostructures,[14−25] such as quantum dots (QDs).[26−37] Confining carriers in the quantum regime leads to widened energy bandgap and blueshift of the PeLED emission color, as demonstrated in the inorganic PbS/PbSe LEDs.[38,39] However, the necessity of preserving ligands to maintain quantum confinement sacrifices carrier injection efficiency.[40,41]

In this work, we grow a high-density array of strongly quantum-confined perovskite ($CsPbBr_3$) nanowires (QPNWs) in nanoporous anodic aluminum oxide (AAO) templates by a low-pressure closed space sublimation (CSS) process. The average diameters of the QPNWs can be precisely tuned by the Al_2O_3 atomic layer deposition (ALD) in the AAO channels to shrink the nanopore size. Specifically, $CsPbBr_3$ QPNWs with diameters of 6.6, 4.3, 3.5, and 2.8 nm are successfully obtained with photoluminescence (PL) emission wavelengths positioned at 512 nm (green), 492 nm (cyan), 481 nm (sky blue),

Received: March 21, 2022
Accepted: April 28, 2022

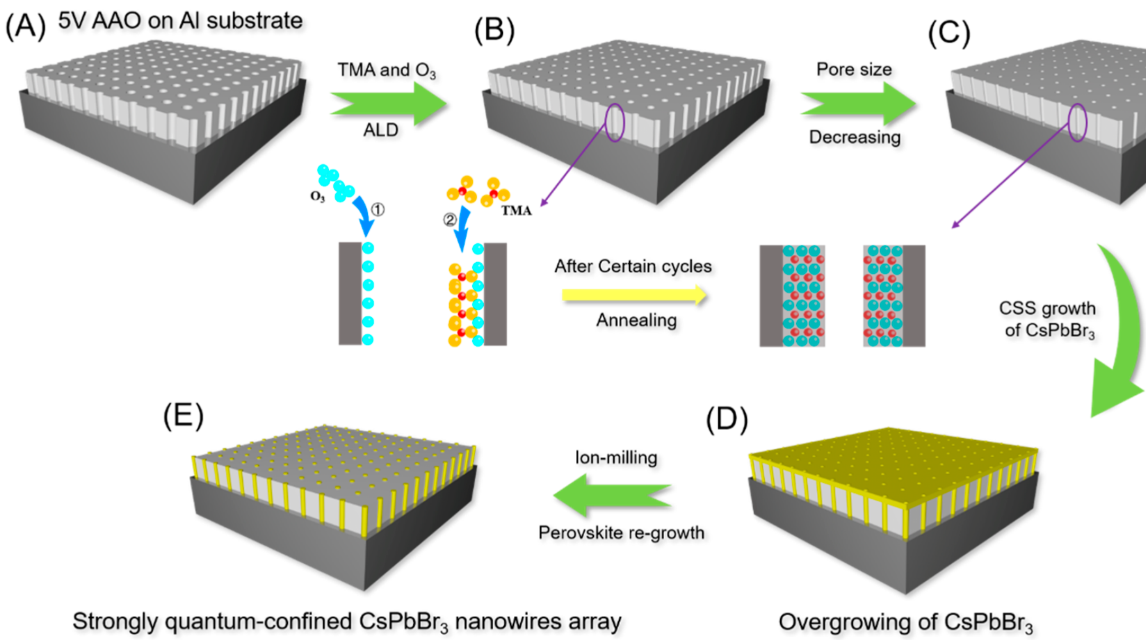

Figure 1. Schematic process flow of the $CsPbBr_3$ QPNWs growth in AAO with tunable pore sizes. (A, B) Deposition of an Al_2O_3 monolayer by the ALD method. (B, C) Pore size decreasing after Al_2O_3 ALD deposition. (C, D) $CsPbBr_3$ QPNW growth inside an AAO channel *via* the CSS method. (D, E) Ion-milling process for surface cleaning.

and 467 nm (pure blue), respectively, demonstrating strong quantum confinement. The PL color tunability *via* the quantum size effect without halide doping exhibits respectable lifetime and color stability with AAO template protection. To further understand the AAO passivation effect and protection mechanism on QPNWs, a systematic study on carrier dynamics and density functional theory (DFT) calculations as for interfaces between perovskites and AAO has been carried out. Finally, QPNW arrays with different diameters are fabricated into PeLEDs with the electroluminescence (EL) emission color changing from green to blue. Intriguingly, the cyan color PeLED could achieve 7.1% external quantum efficiency (EQE), which is the highest for pure $CsPbBr_3$-based cyan blue emission PeLEDs to our best knowledge. Meanwhile the sky-blue and pure-blue emission QPNW LEDs have also been successfully fabricated to demonstrate the feasibility of tunable blue emission. The work here demonstrates the great potential of the QPNWs for high-performance and stable full-color PeLEDs.

RESULTS AND DISCUSSION

Synthesis of $CsPbBr_3$ QPNW Arrays. Figure 1 illustrates the process flow of $CsPbBr_3$ QPNW array fabrication. Initially, AAO with a pore diameter size around 6.6 nm is fabricated with 5 V anodization,[42] which is followed by an ALD Al_2O_3 conformal coating process to decrease the pore size (Figure S4). Afterward, the nanopores in AAO are filled with $CsPbBr_3$ perovskite NWs with different diameters by using a low-pressure CSS process. In case there is a thin layer of $CsPbBr_3$ coating on the top surface of AAO due to NW overgrowth, a surface ion-milling process followed by a short-time regrowth process is carried out. All the experimental details are provided in the Supporting Information. X-ray diffraction analysis (XRD) data of different diameter $CsPbBr_3$ QPNW arrays are obtained to determine the QPNWs' crystal structure. The XRD pattern of QPNWs (Figure S5) grown inside 5 V anodized AAO (0 cycle Al_2O_3 ALD) shows multiple diffraction peaks positioned at 15°, 22.4°, and 30°, which correspond to (100), (110), and (200) lattice planes, respectively. With the increase of the Al_2O_3 ALD cycle and shrinking of the pore size, the diffraction peak of the (110) plane disappears, revealing the QPNW growth confined by the smaller size AAO pore favors formation of (100) oriented monocrystalline NWs. Meanwhile, the full width at half-maximum (FWHM) of diffraction peaks is broadened due to the decreasing of the QPNW diameter. Intriguingly, all diffraction peaks show a gradual shift to larger angles. This can be explained by the shrinking interplanar lattice spacing caused by the stronger physical confinement of QPNWs with the smaller AAO pore sizes.

Morphology and Size Analysis. To further characterize the grown QPNWs, high-resolution scanning electron microscopy (SEM) under the through-the-lens detection (TLD) mode is performed to observe the top-view morphology of QPNWs filled in AAO with a reduced pore size after 15 cycles, 18 cycles, and 20 cycles ALD Al_2O_3 coatings are shown in Figure S6(A−C). A large number of pores (black dots) and QPNWs (white dots) can be seen from Figure S6(A). Although the QPNW filling ratio is not 100%, due to the ultrasmall pore size and challenge of source diffusion, the empty AAO pores will not cause a short-circuit since the AAO sidewall can isolate neighboring QPNWs, which will be discussed later. In Figure S6(B) and (C), as the pore and QPNW size have been reduced beyond the resolution limit of SEM, they cannot be resolved clearly. Therefore, top-view transmission electron microscopy (TEM) images of different diameter QPNWs in an AAO film are obtained and shown in Figure 2(A−C). Note that these images are obtained after scraping the AAO film off the sample, then suspending the broken pieces in alcohol and dropping them on the TEM grid. The black dots marked by circles are vertical QPNWs embedded in AAO, and some QPNWs overlap with each other due to stacking aggregation of broken AAO membranes. We

https://doi.org/10.1021/acsnano.2c02795
ACS Nano XXXX, XXX, XXX−XXX

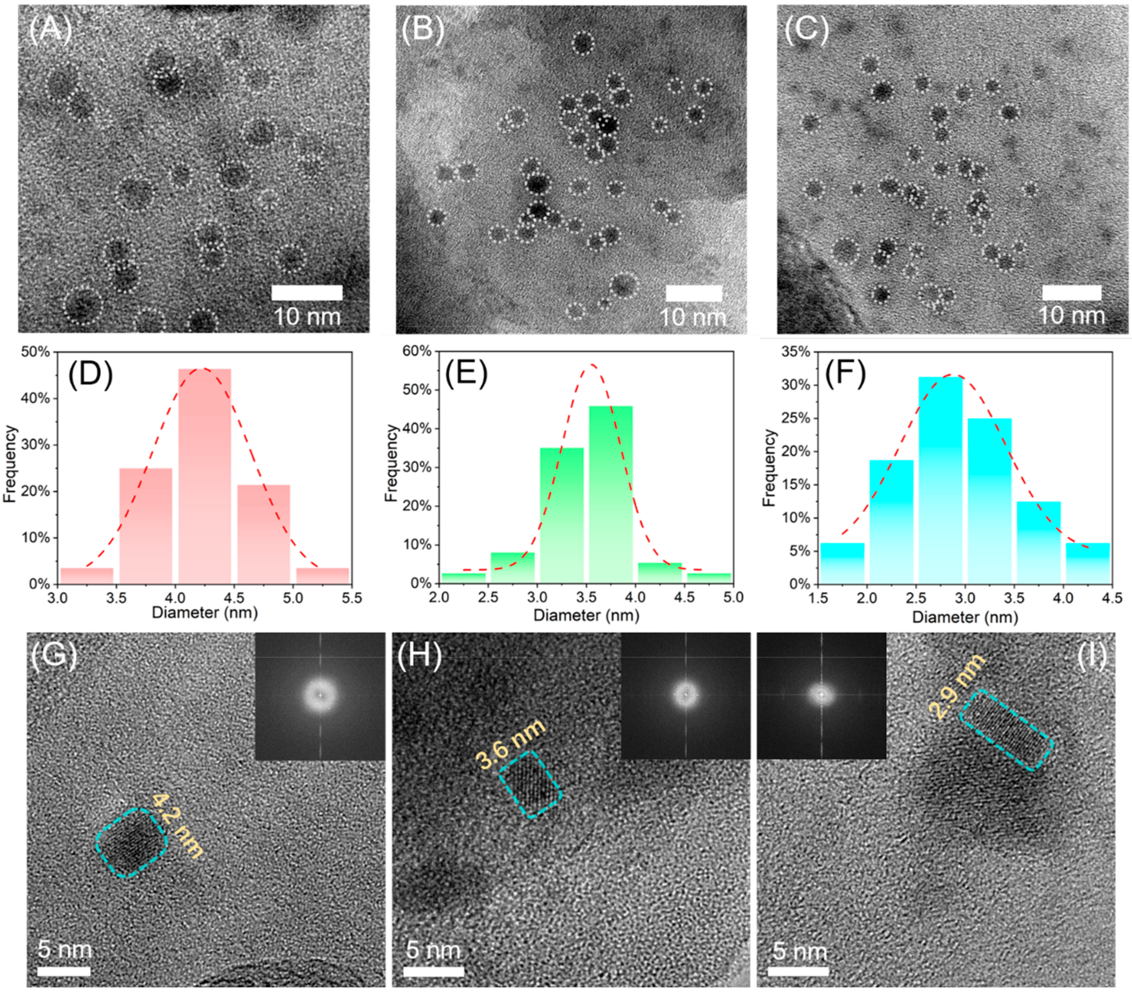

Figure 2. Morphology and size analysis of $CsPbBr_3$ QPNWs with different diameters. TEM images of $CsPbBr_3$ QPNWs grown inside AAO with (A) 15 cycles, (B) 18 cycles, and (C) 20 cycles of ALD coatings. All these QPNWs@AAO samples are scraped off from FTO and milled evenly. (D−F) Size distribution statistics of related TEM image. (G−I) HRTEM images of 4.2, 3.6, and 2.9 nm diameter QPNWs encapsulated in AAO. Inset figures correspond to fast-Fourier-transform (FFT) patterns. All the FFT patterns can be well indexed as the (100) crystal planes of cubic phase $CsPbBr_3$.

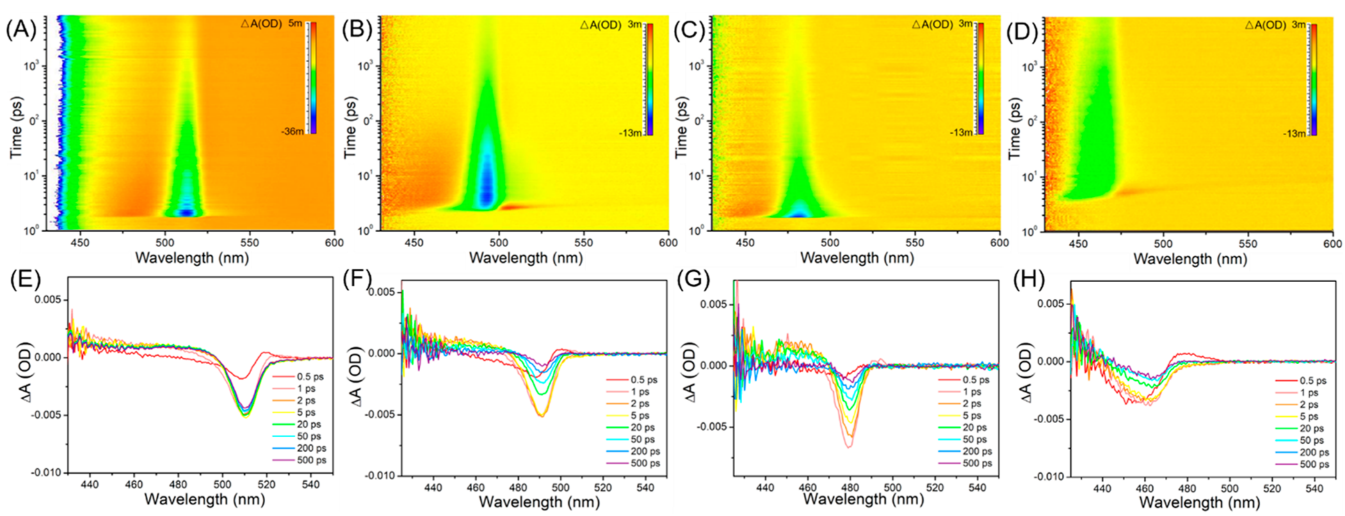

Figure 3. TA measurements of $CsPbBr_3$ QPNWs with different diameters. (A−D) Contour plots of the TA spectrum (QPNWs with diameters of 6.6, 4.3, 3.5, and 2.8 nm, respectively) as a function of wavelength and delay time. (E−H) Related TA spectra at different time scales (0.5, 1, 2, 5, 20, 50, 200, and 500 ps).

https://doi.org/10.1021/acsnano.2c02795
ACS Nano XXXX, XXX, XXX−XXX

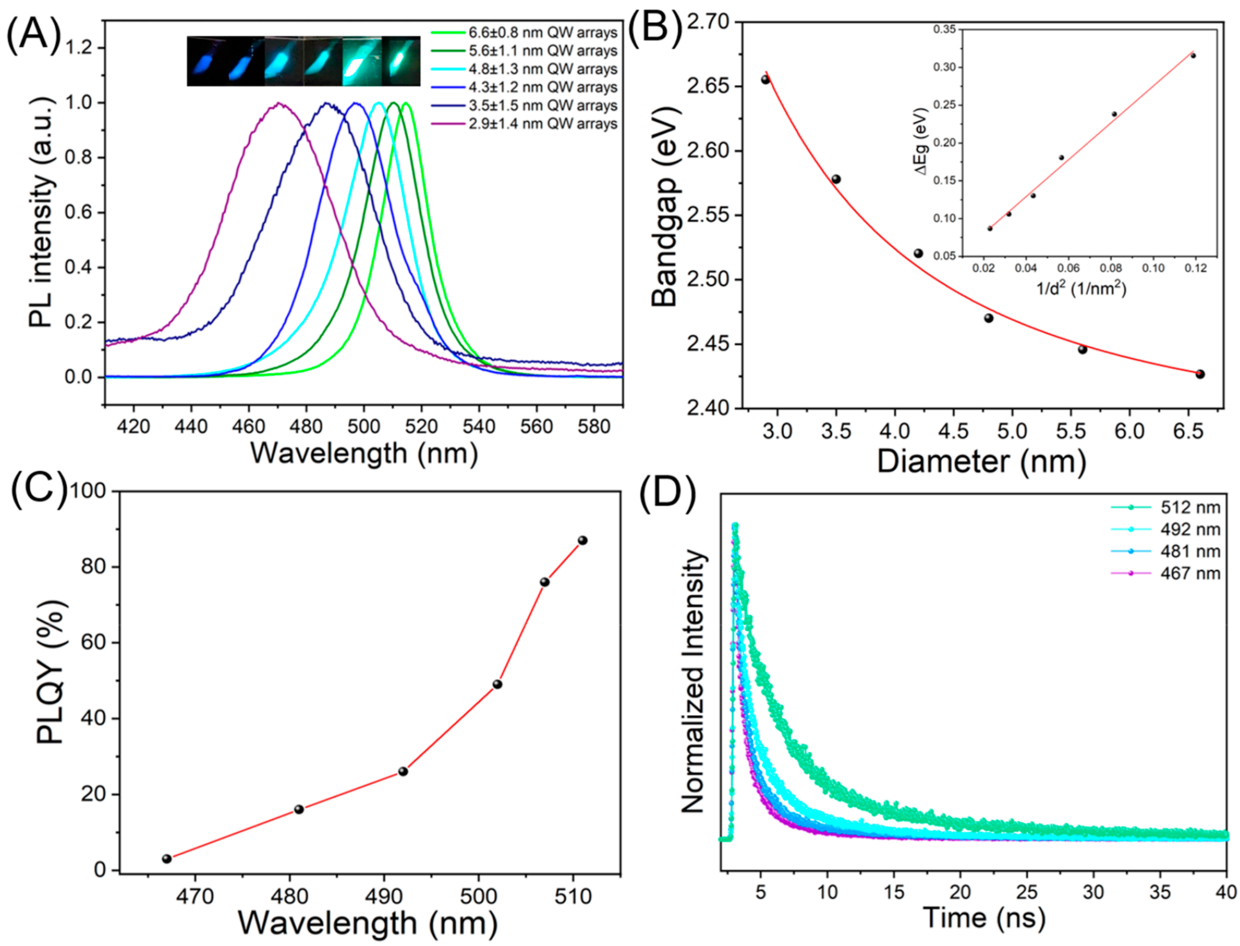

Figure 4. Optical properties of $CsPbBr_3$ QPNWs with different diameters. (A) PL spectrum of $CsPbBr_3$ QPNW arrays grown inside AAO with different diameters. (B) Dependence of bandgaps (eV) *versus* QPNW diameter (nm). The inset figure shows an inverse relationship between bandgap change (ΔE_g) and diameter square ($1/d^2$). (C) PLQYs of different diameter $CsPbBr_3$ QPNW arrays. (D) Time-resolved photoluminescence (TRPL) plots of different diameter $CsPbBr_3$ QPNW arrays.

summarize the size distribution of the interpore distance and calculate the average radial size of QPNWs (Figure 2(D−F)) to be 4.3 nm (15 cycles of ALD), 3.5 nm (18 cycles of ALD), and 2.8 nm (20 cycles of ALD), respectively. As shown in Figure S7, these NW diameters can accommodate maximally six-, five- and four-unit cells of cubic phase $CsPbBr_3$ with a lattice constant around 5.9 Å, along the [010] or [100] directions, at the diameter of the circular pore. High-resolution TEM (HRTEM) of different diameter size QPNWs with clear lattices is shown in Figure 2(G−I). All these lattices within different diameter QPNWs are confirmed to grow along the (100) lattice face by fast-Fourier-transform (FFT) pattern, and the QPNWs are confirmed to be single crystalline, which fits well with the previous XRD result. This result reveals that the AAO nanochannel is guiding the crystal orientation and assisting in epitaxial growth of perovskite QPNWs when the pore size is smaller than 5 nm. It has also been observed that during TEM sample preparation some small pieces of AAO with QPNWs inside and QPNWs came out from AAO pores (Figure S8), which allows us to investigate the crystallinity of individual NWs. Intriguingly, ∼3 nm vertically aligned QPNWs inside bundled AAO with distinctly evident lattice fringes have been observed in Figure S9, and QPNWs are proved to be single-crystalline based on selected area electron diffraction (SAED) (inset image of Figure S9(B)). To show the cross-sectional structure of QPNWs inside AAO more clearly, a lamella of 3.5 nm QPNWs@AAO is prepared by a focus ion-beam (FIB) cutting and milling process, and a false color TEM image (Figure S10(A)) with a related schematic illustration (Figure S10(B)) is exhibited. The total thickness of the AAO layer after 10 min of anodization is around 70 nm, including a barrier layer at the bottom of the AAO channel. Although discontinuous perovskite QPNWs (purple color grains) are melted or even decomposed after high-energy FIB cutting and milling, TEM elemental mapping images (Figure S11) and energy-dispersive X-ray spectroscopy (EDS) elemental analysis (Table S2) prove that perovskite QPNWs are grown inside AAO pores.

Biexciton Effect Observed by TA Analysis. As the kinetics of photocarriers plays a critical role in determining the performance of PeLEDs, two-dimensional contour plots of the Ps-TAS for related 6.6, 4.3, 3.5, and 2.8 nm diameter QPNWs are shown in Figure 3(A−D), respectively. The results show that the center of signals for 6.6, 4.3, 3.5, and 2.8 nm QPNWs are located at 512, 492, 481, and 469 nm, respectively, revealing the diminishing number of radial direction unit cells as the pore size decreases. Besides, the redshift of the signal tail at short time scale (less than 5 ps) indicates a strong biexciton Columbic interaction known as the Stark effect.[33,43] To further investigate the dynamic processes of carriers after photo-

https://doi.org/10.1021/acsnano.2c02795
ACS Nano XXXX, XXX, XXX−XXX

excitation in different diameter QPNWs, transient absorption (TA) spectra at different time resolutions under high-fluence pump laser excitation are shown in Figure 3(E−H). The shape disturbance at the beginning of 1 ps is dominated by hot carrier relaxation after photoexcitation.[34] Afterward, a negative bleaching signal appears with two small positive signals at both sides, and the bleaching signal starts to present a redshift trend with prolonged time. In detail, the spectrum shape of 6.6 nm QPNWs almost remains constant after 5 ps with negligible redshift, while the time to eliminate the redshift and to keep the spectral line shape unchanged becomes longer for smaller diameter QPNWs (20, 50, and 50 ps for 4.3, 3.5, and 2.8 nm QPNWs, respectively). In this period, biexciton characteristics dominate the decay process; the prolonging of decay time with reduction in QPNW diameter reveals the enhanced exciton−exciton interactions. Besides, both the redshift and the fast recovery of bleaching peak can be attributed to the high-energy biexciton induced nonradiative recombination process. Once the biexciton decay is finished, the shape of the spectra remains almost unchanged and only the intensity of the bleaching signal decreases as the decay time lengthens. This process is regarded as exciton radiative recombination. TA spectra of different diameter QPNWs at 50 ps under low-energy pump laser excitation are shown in Figure S12(A), to compare the characteristics of different diameter QPNWs. The blueshift of the bleaching signals is attributed to the strong quantum confinement effect, while the peak broadening with ALD cycle increment is caused by both surface state emission and discrete size distribution, which will be discussed in the text below. The TA kinetics spectrum of different diameter QPNWs is displayed in Figure S12(B). The relaxation time of hot carriers is shorter than 1 ps, which is smaller than the detection limit of our picosecond laser, so that it can be ignored. The short decay time (A_2) and long decay time (A_3) represent the lifetime of double exciton relaxation and exciton radiative recombination (Table S3). The result shows that photon-generated carrier lifetime has a positive correlation with the QPNW diameter. When the diameter of QPNWs decreases, the carrier lifetime is shortened since radiative recombination is suppressed by biexciton interaction, surface defects, and edge dislocations.

PL Color Tunability. Photoluminescence spectra of $CsPbBr_3$ QPNW arrays with different diameters grown in AAO are obtained to show the color tunability (Figure 4(A)). In our previous reports,[42] the PL of $CsPbBr_3$ QPNWs grown inside 5 V AAO exhibits a few nanometer blueshift with surprisingly boosted PLQY up to 90%. Herein, when the pore diameter is further reduced by ALD coating, the PL peak position exhibits a much larger blueshift from the green (512 nm) to the blue (469 nm) region due to enhancement of quantum confinement. Besides, the fwhm of the PL peaks tends to increase as the QPNW diameters shrink (Figure S13(A)). As the ALD Al_2O_3 coating is highly conformal inside the AAO pores, the original pore size variation is preserved and its impact on bandgap is more and more significant when the pore diameter shrinks, due to the quantum size effect. The inset optical images of Figure 4(A) display the corresponding PL color change from green to pure blue, gradually. Figure 4(B) illustrates the dependence of bandgaps *versus* QPNW diameter. The bandgaps are estimated by the PL peak positions, and QPNW diameters are determined by averaged size confirmed in TEM. The inset figure shows an inverse relationship between bandgap change (ΔE_g) and diameter square ($1/d^2$),[44] which is consistent with a standard one-dimensional system of an infinite potential well model:

$$\Delta E_g = \frac{1.17h^2}{8d^2}\cdot\left(\frac{1}{m_e^*}+\frac{1}{m_h^*}\right) = \frac{1.17h^2}{8\mu d^2} = \frac{k}{d^2}$$

Here h, m_e^*, m_h^*, and μ represent Planck's constant, effective mass of electrons and holes, and reduced effective mass, respectively. After substituting the slope value (k) of 2.5 eV nm^{-2} into the function, the reduced effective mass μ is calculated to be $0.176m_0$ (m_0 represents free electron mass), which is slightly larger than the theoretical result value of $0.13m_0$. This result can be attributed to more surface states and edge dislocations created in smaller diameter QPNWs, resulting in the generation of lower energy sub-bands. Figure 4(C) shows the PLQYs of related QPNWs of different diameters. The PLQY monotonically decreases from 88% (6.6 nm) to 77% (5.6 nm), 49% (4.8 nm), 27% (4.3 nm), 16% (3.5 nm), and finally 4% (2.9 nm). We attribute the dropping of PLQYs to the increased defects at the QPNW/AAO interface when reducing the QPNW diameter. Time-resolved photoluminescence (TRPL) plots of different diameter $CsPbBr_3$ QPNW arrays are measured to investigate the PL dynamics directly (Figure 4(D)). The average PL lifetime (τ) decreases from 5.84 ns to 1.4 ns as the diameter of QPNWs becomes smaller, indicating more carrier recombination happens in smaller diameter QPNWs. In detail, all PL decay curves are modeled by biexponential function comprising short-lived (τ_1) and long-lived (τ_2) carrier lifetime, corresponding to nonradiative and radiative recombination. Because of our template-assisted growth, QPNWs are proved to be single crystalline when the diameter is smaller than 4.5 nm and bulk defect density and associated nonradiative recombination rate can be very low. However, both lifetimes are shortened as the QPNW diameter decreases, which suggests both radiative and nonradiative recombination rate are elevated (Table S4). Although the AAO template is reported to be an excellent surface passivation material to metal halide perovskite, the condition of our large surface-to-volume ratio QPNWs is quite different from larger diameter NWs. The quantum confinement becomes stronger when the QPNW diameter reduces so that more photogenerated excitons are created, which promotes the radiative recombination process. However, biexciton interaction happens in the strong quantum confinement regime, leading to more nonradiative recombination. This explanation is also in congruence with previous TA results. Besides, the mismatch between circular pores and cubic structure $CsPbBr_3$ crystals provides more surface states and edge dislocations, which will be discussed in the next section.

Surface-State DFT Calculation and Modeling. To further investigate the influence of symmetry mismatch between AAO pores and perovskite lattice structure, we build three ideal models of 4.3, 3.5, and 2.8 nm diameter QWs, as shown in Figure S7. The diameters are determined by previously discussed TEM results. One (100) plane unit cell thickness along the NW axial orientation is used to simplify the discussion. It is apparent that the ratio of surface unit cell number *versus* the bulk ones increases when the diameter of QPNWs decreases, leading to a more surface state dominated property. To further evaluate the effect of surface state induced electronic structural changes, DFT calculations are carried out, and the computational details and models are summarized in the Supporting Information. To display how the AAO side wall

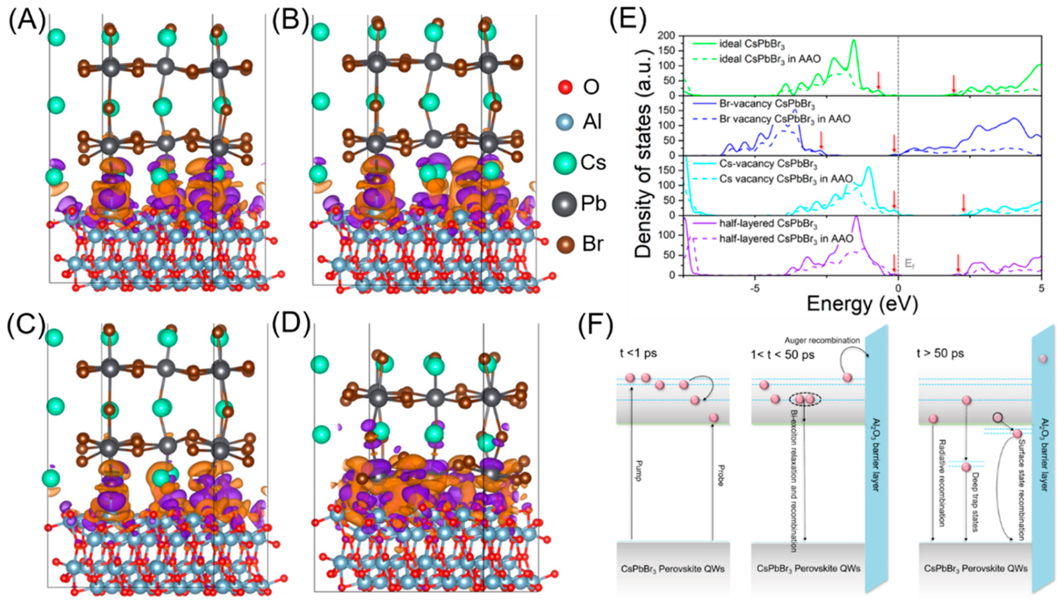

Figure 5. DFT stimulation to illustrate the AAO passivation to surface $CsPbBr_3$ with different kinds of defects. Charge density distribution (CDD) diagrams with different types of defect surfaces. (A) Ideal (pristine) surface. (B) Br-vacancy. (C) Cs-vacancy. (D) Half-layered Pb metallic surface. (E) Corresponding TDOSs of $CsPbBr_3$ perovskite with different kinds of surface states. (F) Schematic of exciton dynamics at different time scales.

can passivate the $CsPbBr_3$ surface, the charge density distribution (CDD) diagrams with different types of defect surfaces are performed (Figure 5(A–D)). In this figure, the purple color and orange color zones are where the electron density is enriched (electrons) and depleted (holes), respectively. It is suggested that a large lattice mismatch of the interface not only results in a more defective environment at the interface but also leads to the presence of a deep trap state within the energy bandgap. However, our calculation shows that the lattice mismatch between $CsPbBr_3$ and Al_2O_3 components is relatively small (3.12%), and no deep trap states appear in the bandgap region of the ideal $CsPbBr_3$/AAO interface. When ideal $CsPbBr_3$ is in contact with the AAO surface, the charge redistribution is delocalized at the interfacial area and is attributed to the Br−Al, Cs−O, and Pb−O bonds. Both electron and hole distributions are dense and partially congruent with the Pb−Br bond orientation of $CsPbBr_3$. Even after one Cs or Br ion at the interface is missing, both charge distribution and delocalization are hardly changed, suggesting that both of these kinds of surface states can be well passivated. However, when a $CsPbBr_3$ unit cell is broken and attached to the AAO surface, the imbalanced electrons and holes in the half-cell of $CsPbBr_3$ impairs the antibonding coupling nature of perovskite, thus making interfacial charge distribution more discrete. Furthermore, more electron-depleted zones are created due to the lack of Pb−Br bonding, which will capture more electrons and further induce charge recombination at the $CsPbBr_3$/AAO interface. The corresponding total density of states (TDOSs) of $CsPbBr_3$ perovskite with different kinds of surface states (ideal (pristine) surface, Cs-vacancy surface, Br-vacancy surface, and half-unit cell surface) in free space and in AAO are shown in Figure 5(E). Owing to the reduction of surface coordination, two small but visible peaks (marked with red arrows) appear above the valence band (VB) and below the conduction band (CB) of free $CsPbBr_3$ surfaces, which can be regarded as surface defects induced trap states. In comparison, after perovskites are grown in the AAO template, new hybrid states are created due to the enhanced interaction between the perovskite and Al_2O_3 layer surface. In addition, density of states of all kinds of $CsPbBr_3$ perovskite surface states passivated with AAO are prone to decrease compared with perovskite without AAO passivation, which contributes to reduction of the density of surface states as well. Moreover, both peaks positioned at VB and CB edges disappear, revealing that the Al_2O_3 surface can passivate the $CsPbBr_3$ surface effectively. In short, the natural Al_2O_3 barrier layer not only can bind with $CsPbBr_3$ strongly but also can passivate an ideal $CsPbBr_3$ surface and ion vacancy defect surface effectively. When the QPNW diameter decreases, an incomplete perovskite unit cell at the QPNW/AAO interface is generated because of shape mismatch with the circular pore shape, as shown in Figure S7. This causes dislocations and deep trap states, and they are more prevalent especially for small-diameter QPNWs. Both factors will cause the generation of higher density of trap states and finally lead to PLQY degradation. A schematic of exciton dynamics at different time scales is shown in Figure 5(F). Biexciton recombination and Auger recombination processes happen at short time scales, while surface state recombination and deep trap state induced nonradiative recombination take place at long time scales so that the lifetime of T_3 will be shortened.

QPNW Array Based PeLEDs. Although blue PeLEDs have been reported with the utilization of ultrathin perovskite nanoplatelets (NPs) synthesized by the hot-injection method,[16,45] the device performance is still not satisfactory due to the poorly passivated interface, NP aggregation in the thin film induced PLQY plummeting issue, and inferior charge injection efficiency. Considering that our vertically aligned $CsPbBr_3$ QPNW arrays are well passivated and isolated from adjacent NWs by the AAO template, which can significantly improve the stability against O_2 and moisture and also thwart the aggregation issue, they are fabricated into PeLEDs with much improved EL color stability. Figure 6(A) shows a schematic of

https://doi.org/10.1021/acsnano.2c02795
ACS Nano XXXX, XXX, XXX−XXX

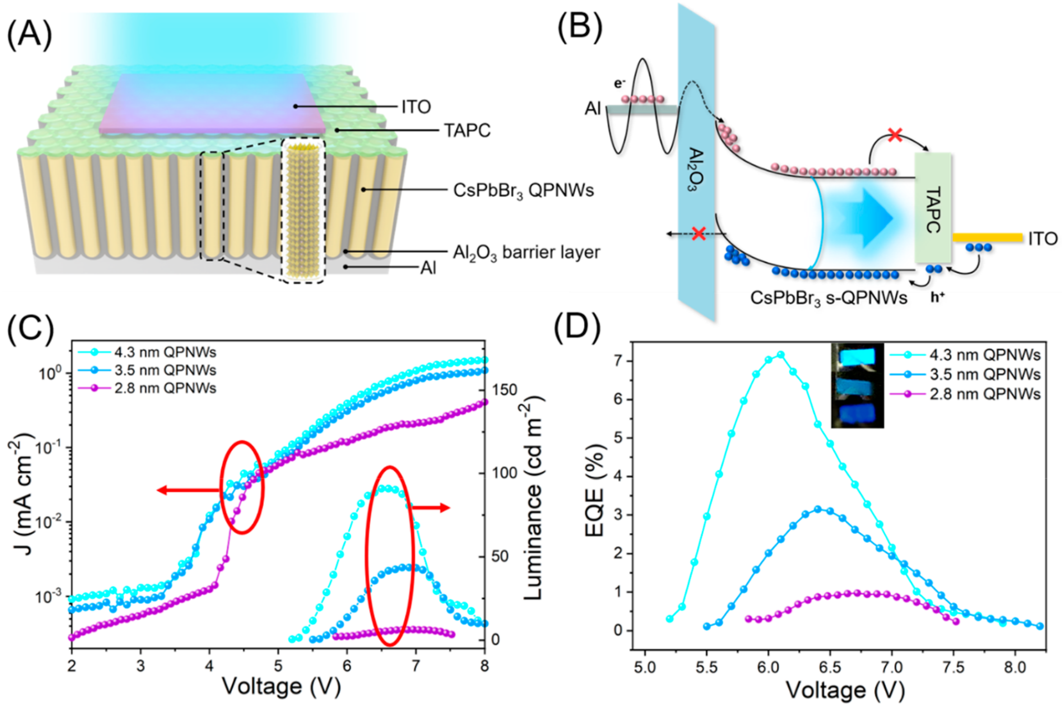

Figure 6. PeLEDs based on QPNWs with tunable emission. (A) Schematic of the QPNW array based PeLED device structure. (B) Band alignment of the device under bias voltage. (C) Current density−voltage−luminance (*J*−*V*−*L*) curves of different colored PeLEDs. (D) Related EQE curves of different colored PeLEDs.

our PeLED device structure. The Al chip at the bottom acts as a cathode, on top of which there are QPNW arrays laterally encapsulated by the AAO. It is worth noting that an ultrathin Al_2O_3 barrier layer exists between Al and $CsPbBr_3$ QPNWs, and the thickness varies as the cycles of ALD coating change (Figure S10(A) and Figure S11). Then, a thin layer (∼25 nm) of 1,1-bis[(di-4-tolylamino)phenyl]cyclohexane (TAPC) is spin-coated onto the QPNWs to serve as a hole-injection and electron-blocking layer. Finally, a 100 nm thick transparent indium tin oxide (ITO) electrode is sputtered as the top anode, and EL light is extracted from this side. Figure 6(B) shows the band alignment of a working device under bias voltage. The electron injection mechanism is considered as a standard metal−insulator−semiconductor (MIS) junction with a device architecture comprising Al/Al_2O_3 barrier layer/perovskite QPNWs. When low bias is applied between the ITO anode and Al cathodes, holes are injected into QPNWs *via* the TAPC layer, while the energy band of perovskite QPNWs near Al_2O_3 bends upward and electrons are blocked and accumulated near the Al side. As the bias becomes larger, electrons tunnel through the Al_2O_3 thin layer and radiatively recombine with holes to achieve photon emission. The current density−voltage−luminance (*J*−*V*−*L*) curves of different color PeLEDs based on different diameter $CsPbBr_3$ QPNWs are shown in Figure 6(C). The turn-on voltages elevate (from 5.2, to 5.4 V, to 5.7 V) as the bandgap of emissive $CsPbBr_3$ QPNWs increases from 2.52 eV (cyan), to 2.58 eV (sky blue), to 2.65 eV (pure blue), while the working current density at the same driving voltage decreases when $CsPbBr_3$ QPNW based PeLEDs have more blue-shifted EL emission. This result can be attributed to hindered electron tunneling by a thicker Al_2O_3 barrier after ALD coating and lower carrier density inside the smaller volume QPNWs. Besides, the leakage current density is quite small, revealing that charge injection is well balanced and the QPNWs/TAPC interface is well passivated with good contact. This result is proven by a cross-sectional SEM image as well (Figure S14). Moreover, the maximum luminances of cyan (96 cd/m^2), sky-blue (47 cd/m^2), and pure-blue (13 cd/m^2) color PeLEDs are operated at 6.5, 6.8, and 7 V (Figure 6(D)), respectively. Related EL spectra are shown in Figure S15. We deem that the deep trap states stemming from the crystal dislocations at $CsPbBr_3$/AAO interfaces, which we mentioned before, account for the low luminance level and EQE degradation. To further understand how charge injection through different surface states influences the EL performance, we introduce a free electron at the $CsPbBr_3$/AAO interface to stimulate the charge injection process in the DFT simulation (Figures S16 and S17.). Compared with the ideal $CsPbBr_3$/AAO interface model, charge distribution of the Br-vacancy $CsPbBr_3$/AAO interface does not show an obvious change after excessive electrons are introduced. As for Cs-vacancy and half-layered $CsPbBr_3$/AAO interfaces, most of the electrons are restricted at the interface or inside the AAO layer. TDOS plots after electron injection, as shown in Figure S18, suggest that only Fermi levels shift to higher energy instead of a new surface state appearing after electron injection. All this evidence indicates that the excellent device performance for cyan-colored PeLEDs derives from the effective passivation of AAO, and more electrons are wasted inside the AAO barrier layer or at the interface instead of being injected into the perovskite emitter in smaller diameter QPNWs. As a result, the cyan-colored PeLEDs with moderate surface states and less surface defects could achieve 7.1% EQE, and the PeLEDs of sky-blue emission and pure-blue color emission PeLEDs are demonstrated with 3.2% and 0.9% EQE as well. Although the performances of sky-blue and pure-blue color PeLEDs still fall behind due to shape mismatch between circular pores and cubic phase perovskites, AAO templates

https://doi.org/10.1021/acsnano.2c02795
ACS Nano XXXX, XXX, XXX−XXX

with square pores can be achieved by the nanoimprinting process to diminish the surface defects and thus improve device performance in the near future.[46]

CONCLUSION

In this work, an ALD coating method is utilized to further decrease the ultrasmall pore size of AAO down to the few nanometer range, and a template-assisted one-step CSS growth method has been developed to grow $CsPbBr_3$ QPNW arrays in the AAO templates. When decreasing the QPNWs' diameter from 6 nm to 2.8 nm, the PL peak is significantly shifted from 512 nm to 467 nm, demonstrating a strong quantum confinement effect. Theoretical calculations show that the AAO sidewalls can passivate halide and cation vacancies effectively. QPNW array based PeLEDs have been fabricated with EL emission covering the cyan, sky-blue, and pure-blue spectral range. Benefiting from efficient charge injection in the vertically one-dimensional structure, 7.1% EQE for 492 nm emission has been achieved as the state-of-the-art for $CsPbBr_3$-based cyan-colored PeLEDs, while the EQEs of sky-blue and pure-blue PeLEDs have been achieved as 3.2% and 0.9% with room to optimize in the future. Our exploration here demonstrates a distinctive approach to nanoengineer the dimensions and optical propertyies of low-dimensional perovskites and also the great potential of QPNWs for high-performance and stable full-color PeLEDs in the future.

METHODS

AAO Template Fabrication. The AAO was fabricated by a well-known anodic anodization process at low voltage. In brief, a high-purity aluminum chip with 1.5 × 2.5 cm^2 size was cleaned with acetone and isopropyl alcohol (IPA) first, then electrochemically polished in solution with 25 vol % $HClO_4$ and 75 vol % CH_3CH_2OH for 2.5 min under 14 V at 10 °C. Afterward, an overnight first anodization process was carried out by immersing the Al chip in a 5 vol % sulfuric acid aqueous solution under 5 V in direct current (DC) mode at 1 °C. Then an acid etching (6 wt % H_3PO_4 and 1.8 wt % CrO_3) process was carried out at 98 °C for 30 min to etch away the first, low-quality anodized AAO film, followed by a 10 or 20 min (around 100 and 200 nm thick, respectively) second anodization with the same conditions as the first anodization. Finally, a semiordered high-quality AAO film was directly fabricated on the Al chip. For a highly transparent AAO film fabricated on fluorine-doped tin oxide (FTO) glass, a similar two-step anodization process was executed. First, FTO glass was cleaned in sequence with Triton X-100, water, IPA, acetone, and IPA, then blown-dry by a nitrogen gun. Afterward, 500 nm thick Al was sputtered onto an FTO substrate, followed by a first, 1 h anodization and etching process by phosphoric acid solution (2.8 mL + 80 mL of H_2O) at 35 °C for 6 h. Then, a second anodization was performed until all the Al was anodized into a highly transparent AAO film.

AAO Pore Size Shrinking by ALD Coating. The nanoporous AAO membranes were coated by Al_2O_3 ALD by an ALD reactor operated in a quasi-static mode at 200 °C. The AAO membranes on an Al or FTO substrate were placed in the chamber, and the distance to the carrier source gas flow was about 5 cm with an angle of 15 degrees to the chamber ground. The chamber was evacuated to vacuum by a mechanical pump after samples were placed inside; then trimethyl aluminum (TMA, Aldrich) and ozone (O_3) were alternately exposed into the chamber during the coating process, followed by a long wait time held for gas-state source diffusion into the narrow pores, then a long purge time to evacuate the chamber and to the clean source residue by nitrogen. Certain cycles of the ALD process were carried out to realize a pore size diameter that decreased controllably. Detailed parameters for ALD are exhibited in Table S1.

$CsPbBr_3$ QPNW Growth by the Close Space Sublimation Method. The QPNW growth was followed by a CSS method, and the process flow is shown in Figure S1. Briefly, we mixed CsBr with $PbBr_2$ in 3:1 mol ratio; then the mixed powder was milled in a mortar until the white-colored powder changed to yellow. Then we put the precursor powder into a quartz boat and transferred it into a large-diameter (4 cm) quartz tube right on top of the heating source, while the empty AAO was stuck on the other side, which was far away from the heat source. The quartz tube was connected to a vacuum pump and well-sealed. Before heating the source, a degassing process with a gas pressure below 10^{-5} Torr was needed to get rid of air inside the AAO pore. After a long (more than 15 min) degassing time, the air inside the AAO pores can be pumped out thoroughly. Then, the precursor was heated with a rate of 5 °C per minute, and the pressure inside the chamber was also released at a rate of 2 × 10^{-5} Torr per minute. When the precursor was heated to 400 °C, the source vapor can be evaporated as the pressure inside the chamber keeps increasing simultaneously, so that the perovskite precursor would be pumped out and filled inside the AAO pores by chance owing to the pressure difference between the chamber and AAO pores. Remember that the temperature at the AAO substrate side was much lower than the source side so that the precursor will cool and recrystallize inside the AAO pore and NWs could keep growing and accumulate as the precursor vapor comes out. Finally, the 100 nm thick AAO template was fully filled with perovskite, and vertically aligned $CsPbBr_3$ QPNW arrays inside the AAO template were obtained. Nevertheless, there would be a layer of perovskite thin film covering the AAO membrane so that an ion-milling process was performed in a vacuum of 1.4 × 10^{-4} Torr with argon ions accelerated at 300 V for 40 min to remove the redundant perovskite thin layer if necessary.

TEM and FIB Lamella Preparation. The TEM sample showing mostly a "dots" morphology refers to the radial direction of QPNWs encapsulated inside AAO being simply scratched off from the FTO/glass and pulverized with the aid of a mortar−pestle, followed by dispersion in toluene. Afterward, the dispersion was dropped onto a TEM copper grid for further observation. The fabrication of the lamella for TEM imaging was carried out using a dual-beam FIB/FESEM system (FEI Helios G4 UX) containing both a focused Ga^+ ion beam and an ultra-high-resolution field emission scanning electron column that can be used in synchrony.

Characterization. SEM images were characterized using a field-emission scanning electron microscope under TLD detection mode in an FIB−SEM system (FEI Helios G4 UX). The imaging and EDS study of the NWs were done using a transmission electron microscope JEM 2010 (JEOL). FIB cutting was operated in the FEI Helios G4 UX FIB-SEM system. XRD patterns were obtained using a Bruker D8 X-ray diffractometer. Transient absorption measurements were detected by equipping a regeneratively amplified Ti:sapphire laser source (Coherent Legend, 800 nm, 150 fs, 5 mJ per pulse, and 1 kHz repetition rate) and Helios (Ultrafast Systems LLC) spectrometers. A portion of the 800 nm output (75%) pulse was frequency-doubled in a BaB_2O_4 (BBO) crystal, which could generate 400 nm pump light; meanwhile the remaining portion of the output was concentrated into a sapphire window to produce white light continuum (420−780 nm) probe light. The 400 nm pump beam was focused on the sample with a beam waist of about ∼360 μm, and the power intensity was fixed at 40 μJ cm^{-2} in this experiment. PL including the spectrum and lifetime were measured using a Varian Cary 500 spectrometer (Varian, USA) and an Edinburgh FS5 fluorescence spectrometer, respectively. The PLQY was measured using a custom-built micro-PL instrument reported by us before. The LED devices were driven by an HP 4156A analyzer along with a probe station (Sigatone, USA). Luminance and EQE were measured with an Ocean Optics Flame spectrometer.

Computational Methods and Models. All calculations were carried out by using the Vienna Ab initio Simulation Package (VASP)[47−50] within the DFT framework. The Perdew−Burke−Ernzerhof (PBE) functional[51] was applied to treat the exchange−correlation energy. The projector augmented wave (PAW)[52] was applied, and the energy cutoff was 400 eV. The sampling over the Brillouin zone for bulk Al_2O_3, $CsPbBr_3$ and $CsPbBr_3$ surfaces, and

https://doi.org/10.1021/acsnano.2c02795
ACS Nano XXXX, XXX, XXX−XXX

$CsPbBr_3/Al_2O_3$ composites was treated by the Monkhorst−Pack technique,[53] and the (6 × 6 × 6), (6 × 6 × 6), (2 × 2 × 1), and (2 × 2 × 1) grids were applied, respectively. The geometry optimization process was repeated until the energy change of the ionic steps is less than 10^{-5} eV and the force on the atoms less than 0.05 eV/Å. Furthermore, dispersion interactions were treated on the DFT-D3 level.[54,55] For the surface and composite models, a vacuum slab of 15 Å was introduced to avoid the pseudointeraction along periodic images along the *z*-axis. The crystal models of Al_2O_3 and $CsPbBr_3$ are depicted in Figure S2.

According to the optimized lattice constants of the Al_2O_3 primary cell (5.147 Å) and $CsPbBr_3$ (5.192 Å), it can be found that the (110) $-(\sqrt{2}\times\sqrt{2})$ surface of the Al_2O_3 primary cell well matches the (100) $-(\sqrt{5}\times\sqrt{5})$ one of $CsPbBr_3$, and the lattice mismatch between the two components is 3.12%, indicating stable interfaces can be formed between them. Furthermore, to evaluate the bonding strength of the interfaces, the bonding energy (E_{bd}) is calculated according to the following equation:

$$E_{bd} = E_{CsPbBr_3/Al_2O_3} - E_{Al_2O_3} - E_{CsPbBr_3}$$

where E_{CsPbBr_3/Al_2O_3}, $E_{Al_2O_3}$, and E_{CsPbBr_3} are the total energies of optimized $CsPbBr_3/Al_2O_3$ interfaces, Al_2O_3 slabs, and $CsPbBr_3$ slabs. Furthermore, four (001) $-(\sqrt{5}\times\sqrt{5})$ surfaces of $CsPbBr_3$ were considered and are shown in Figure S3.

PeLED Device Fabrication. PeLEDs were further fabricated based on QPNWs grown on an Al substrate. The hole-injection electron-blocking material TAPC was diluted in toluene (10 mg/mL) and stirred overnight. Then, 70 μL of TAPC solution was dropped on top of AAO filled with $CsPbBr_3$ QPNWs and spin-coated at 3500 rpm for 1 min. Afterward, a 100 nm thick transparent ITO electrode was sputtered with a rectangle-shaped shadow mask of 0.12 cm^2 area for light extraction.

ASSOCIATED CONTENT

Supporting Information

The Supporting Information is available free of charge at https://pubs.acs.org/doi/10.1021/acsnano.2c02795.

Experimental procedures, computational models, additional SEM and TEM images, XRD spectra, schematics for ideal models, additional TA results, characteristics of different diameter QPNWs with PL stability, EL spectrum, additional CDD diagrams and TDOSs results, ALD parameters, EDS results, TA lifetime, PL lifetime, and device performance comparison with other reports (PDF)

AUTHOR INFORMATION

Corresponding Author

Zhiyong Fan − *Department of Electronic and Computer Engineering, The Hong Kong University of Science and Technology, Kowloon, Hong Kong SAR 999077, China; State Key Laboratory of Advanced Displays and Optoelectronics Technologies and Guangdong-Hong Kong-Macao Joint Laboratory for Intelligent Micro-Nano Optoelectronic Technology, HKUST, Kowloon, Hong Kong SAR 999077, China*; orcid.org/0000-0002-5397-0129; Email: eezfan@ust.hk

Authors

Yu Fu − *Department of Electronic and Computer Engineering, The Hong Kong University of Science and Technology, Kowloon, Hong Kong SAR 999077, China; State Key Laboratory of Advanced Displays and Optoelectronics Technologies and Guangdong-Hong Kong-Macao Joint Laboratory for Intelligent Micro-Nano Optoelectronic Technology, HKUST, Kowloon, Hong Kong SAR 999077, China*

Swapnadeep Poddar − *Department of Electronic and Computer Engineering, The Hong Kong University of Science and Technology, Kowloon, Hong Kong SAR 999077, China*

Beitao Ren − *Department of Electronic and Computer Engineering, The Hong Kong University of Science and Technology, Kowloon, Hong Kong SAR 999077, China*

Ying Xie − *School of Chemistry and Materials Science, Heilongjiang University, Harbin 150080 Heilongjiang, China*

Qianpeng Zhang − *Department of Electronic and Computer Engineering, The Hong Kong University of Science and Technology, Kowloon, Hong Kong SAR 999077, China*

Daquan Zhang − *Department of Electronic and Computer Engineering, The Hong Kong University of Science and Technology, Kowloon, Hong Kong SAR 999077, China*

Bryan Cao − *Department of Electronic and Computer Engineering, The Hong Kong University of Science and Technology, Kowloon, Hong Kong SAR 999077, China*

Yunqi Tang − *School of Energy and Environment, City University of Hong Kong, Kowloon Tong, Hong Kong SAR 999077, China*

Yucheng Ding − *Department of Electronic and Computer Engineering, The Hong Kong University of Science and Technology, Kowloon, Hong Kong SAR 999077, China*

Xiao Qiu − *Department of Electronic and Computer Engineering, The Hong Kong University of Science and Technology, Kowloon, Hong Kong SAR 999077, China*

Lei Shu − *Department of Electronic and Computer Engineering, The Hong Kong University of Science and Technology, Kowloon, Hong Kong SAR 999077, China*

Jin-Feng Liao − *MOE Key Laboratory of Bioinorganic and Synthetic Chemistry, Lehn Institute of Functional Materials, School of Chemistry, Sun Yat-sen University, Guangzhou 510217 Guangdong, China*

Dai-Bin Kuang − *MOE Key Laboratory of Bioinorganic and Synthetic Chemistry, Lehn Institute of Functional Materials, School of Chemistry, Sun Yat-sen University, Guangzhou 510217 Guangdong, China*; orcid.org/0000-0001-6773-2319

Complete contact information is available at: https://pubs.acs.org/10.1021/acsnano.2c02795

Author Contributions

Z.F. and Y.F. conceptualized the experiments and analyzed the results. Y.F. carried out the $CsPbBr_3$ QPNW preparation, device fabrication, and most of the detailed structural, optical, and electrical characterizations. S.P. worked on TEM-FIB fabrication of the lamella and all TEM imaging. B.R. helped with sample preparation and device optimization. Y.X. performed the DFT simulation. Q.Z., D.Z., B.C., Y.T., L.S., J.L., and D.K. helped with characterization. Y.D. and X.Q. worked on schematic drawings of materials and the device structure. All authors participated in manuscript writing and articulation.

Funding

This work was financially aided by General Research Fund (Project Nos. 16205321, 16309018, 16214619) from the Hong Kong Research Grant Council, Innovation Technology Commission Fund (Project No. GHP/014/19SZ), the HKUST Fund of Nanhai (Grant No. FSNH-18FYTRI01), and Shenzhen Science and Technology Innovation Commission (Project Nos. JCYJ20180306174923335, JCYJ20170818114107730).

Notes

The authors declare no competing financial interest.

ACKNOWLEDGMENTS

The authors thank Prof. Sam H. Y. Hsu, School of Energy and Environment, City University of Hong Kong, for helping with the material characterization. The authors express gratitude to Mr. Qi Li, Department of Chemistry, Heilongjiang University, for detailed discussions and providing suggestions on DFT calculations. The authors also thank Ms. Yan Zhang, Mr. Alex H. K. Wong, Dr. Roy Ho, and Dr. Yuan Cai from Material and Characterization and Preparation Facility, The Hong Kong University of Science and Technology, for technical assistance with the SEM, TEM, and FIB.

REFERENCES

(1) Protesescu, L.; Yakunin, S.; Bodnarchuk, M. I.; Krieg, F.; Caputo, R.; Hendon, C. H.; Yang, R. X.; Walsh, A.; Kovalenko, M. V. Nanocrystals of cesium lead halide perovskites ($CsPbX_3$, X= Cl, Br, and I): novel optoelectronic materials showing bright emission with wide color gamut. *Nano Lett.* **2015**, *15*, 3692−3696.

(2) Kovalenko, M. V.; Protesescu, L.; Bodnarchuk, M. I. Properties and potential optoelectronic applications of lead halide perovskite nanocrystals. *Science* **2017**, *358*, 745−750.

(3) Cho, H.; Jeong, S.-H.; Park, M.-H.; Kim, Y.-H.; Wolf, C.; Lee, C.-L.; Heo, J. H.; Sadhanala, A.; Myoung, N.; Yoo, S. Overcoming the electroluminescence efficiency limitations of perovskite light-emitting diodes. *Science* **2015**, *350*, 1222−1225.

(4) Shi, D.; Adinolfi, V.; Comin, R.; Yuan, M.; Alarousu, E.; Buin, A.; Chen, Y.; Hoogland, S.; Rothenberger, A.; Katsiev, K. Low trap-state density and long carrier diffusion in organolead trihalide perovskite single crystals. *Science* **2015**, *347*, 519−522.

(5) Tan, Z.-K.; Moghaddam, R. S.; Lai, M. L.; Docampo, P.; Higler, R.; Deschler, F.; Price, M.; Sadhanala, A.; Pazos, L. M.; Credgington, D. Bright light-emitting diodes based on organometal halide perovskite. *Nat. Nanotechnol.* **2014**, *9*, 687−692.

(6) Hassan, Y.; Park, J. H.; Crawford, M. L.; Sadhanala, A.; Lee, J.; Sadighian, J. C.; Mosconi, E.; Shivanna, R.; Radicchi, E.; Jeong, M. Ligand-engineered bandgap stability in mixed-halide perovskite LEDs. *Nature* **2021**, *591*, 72−77.

(7) Knight, A. J.; Herz, L. M. Preventing phase segregation in mixed-halide perovskites: a perspective. *Energy Environ. Sci.* **2020**, *13*, 2024−2046.

(8) Yoon, Y. J.; Jin, Y. K. A recent advances of blue perovskite light emitting diodes for next generation displays. *J. Semicond.* **2021**, *42*, 148−159.

(9) Xing, J.; Zhao, Y.; Askerka, M.; Quan, L. N.; Gong, X.; Zhao, W.; Zhao, J.; Tan, H.; Long, G.; Gao, L. Color-stable highly luminescent sky-blue perovskite light-emitting diodes. *Nat. Commun.* **2018**, *9*, 3541.

(10) Ochsenbein, S. T.; Krieg, F.; Shynkarenko, Y.; Rainò, G.; Kovalenko, M. V. Engineering color-stable blue light-emitting diodes with lead halide perovskite nanocrystals. *ACS Appl. Mater. Interfaces.* **2019**, *11*, 21655−21660.

(11) Zou, G.; Li, Z.; Chen, Z.; Chu, L.; Yip, H. L.; Cao, Y. Color-Stable Deep-Blue Perovskite Light-Emitting Diodes Based on Organotrichlorosilane Post-Treatment. *Adv. Funct. Mater.* **2021**, *31*, 2103219.

(12) Fan, Z.; Chen, Y.; Lin, Y.; Zi, Y.; Ko, H.; Zhang, Q. Preface to the Special Issue on Flexible Energy Devices. *J. Semicond.* **2021**, *42*, 100101.

(13) Wang, Y.; Quintana, X.; Kim, J.; Guan, X.; Hu, L.; Lin, C.-H.; Jones, B. T.; Chen, W.; Wen, X.; Gao, H.; Wu, T. Phase segregation in inorganic mixed-halide perovskites: from phenomena to mechanisms. *Photonics Res.* **2020**, *8*, 11000A56.

(14) Malgras, V.; Tominaka, S.; Ryan, J. W.; Henzie, J.; Takei, T.; Ohara, K.; Yamauchi, Y. Observation of quantum confinement in monodisperse methylammonium lead halide perovskite nanocrystals embedded in mesoporous silica. *J. Am. Chem. Soc.* **2016**, *138*, 13874−13881.

(15) Demchyshyn, S.; Roemer, J. M.; Groiß, H.; Heilbrunner, H.; Ulbricht, C.; Apaydin, D.; Böhm, A.; Rütt, U.; Bertram, F.; Hesser, G. Confining metal-halide perovskites in nanoporous thin films. *Sci. Adv.* **2017**, *3*, No. e1700738.

(16) Hoye, R. L.; Lai, M.-L.; Anaya, M.; Tong, Y.; Gałkowski, K.; Doherty, T.; Li, W.; Huq, T. N.; Mackowski, S.; Polavarapu, L. Identifying and reducing interfacial losses to enhance color-pure electroluminescence in blue-emitting perovskite nanoplatelet light-emitting diodes. *ACS Energy Lett.* **2019**, *4*, 1181−1188.

(17) Zhu, Y.; Zhang, Q.; Shu, L.; Zhang, D.; Fan, Z. Recent progress of efficient flexible solar cells based on nanostructures. *J. Semicond.* **2021**, *42*, 101604.

(18) Ashley, M. J.; Kluender, E. J.; Mirkin, C. A. Fast Charge Extraction in Perovskite-Based Core-Shell Nanowires. *ACS Nano* **2018**, *12*, 7206−7212.

(19) Fu, Y.; Zhu, H.; Stoumpos, C. C.; Ding, Q.; Wang, J.; Kanatzidis, M. G.; Zhu, X.; Jin, S. Broad wavelength tunable robust lasing from single-crystal nanowires of cesium lead halide perovskites (CsPbX3, X= Cl, Br, I). *ACS Nano* **2016**, *10*, 7963−7972.

(20) Kumar, S.; Jagielski, J.; Yakunin, S.; Rice, P.; Chiu, Y.-C.; Wang, M.; Nedelcu, G.; Kim, Y.; Lin, S.; Santos, E. J. Efficient blue electroluminescence using quantum-confined two-dimensional perovskites. *ACS Nano* **2016**, *10*, 9720−9729.

(21) Yin, W.; Li, M.; Dong, W.; Luo, Z.; Li, Y.; Qian, J.; Zhang, J.; Zhang, W.; Zhang, Y.; Kershaw, S. V. Multidentate Ligand Polyethylenimine Enables Bright Color-Saturated Blue Light-Emitting Diodes Based on CsPbBr3 Nanoplatelets. *ACS Energy Lett.* **2021**, *6*, 477−484.

(22) Zhou, H.; Yuan, S.; Wang, X.; Xu, T.; Wang, X.; Li, H.; Zheng, W.; Fan, P.; Li, Y.; Sun, L. Vapor growth and tunable lasing of band gap engineered cesium lead halide perovskite micro/nanorods with triangular cross section. *ACS Nano* **2017**, *11*, 1189−1195.

(23) Zhang, D.; Zhang, Q.; Ren, B.; Zhu, Y.; Abdellah, M.; Fu, Y.; Cao, B.; Wang, C.; Gu, L.; Ding, Y.; Tsui, K.-H.; Fan, S.; Poddar, S.; Shu, L.; Zhang, Y.; Kuang, D.-B.; Liao, J.-F.; Lu, Y.; Zheng, K.; He, Z.; Fan, Z. Large-scale planar and spherical light-emitting diodes based on arrays of perovskite quantum wires. *Nat. Photonics* **2022**, *16*, 284−290.

(24) Huang, H.; Lu, L.; Wang, J.; Jie, Y.; Leung, S. F.; Wang, Y.; Di, C.; Chen, X.; Shen, G.; Li, D. Performance enhancement of thin-film amorphous silicon solar cells with low cost nanodent plasmonic substrates. *Energy Environ. Sci.* **2013**, *6*, 2965−2971.

(25) Chueh, Y. L.; Ford, A. C.; Ho, J. C.; Jacobson, Z. A.; Javey, A. Formation and Characterization of NixInAs/InAs Nanowire Heterostructures by Solid Source Reaction. *Nano Lett.* **2008**, *8*, 4528.

(26) Ma, D.; Lin, K.; Dong, Y.; Choubisa, H.; Proppe, A. H.; Wu, D.; Wang, Y.-K.; Chen, B.; Li, P.; Fan, J. Z. Distribution control enables efficient reduced-dimensional perovskite LEDs. *Nature* **2021**, *599*, 594−598.

(27) Deng, W.; Xu, X.; Zhang, X.; Zhang, Y.; Jin, X.; Wang, L.; Lee, S. T.; Jie, J. Organometal halide perovskite quantum dot light-emitting diodes. *Adv. Funct. Mater.* **2016**, *26*, 4797−4802.

(28) Jiang, M.; Hu, Z.; Liu, Z.; Wu, Z.; Ono, L. K.; Qi, Y. Engineering green-to-blue emitting CsPbBr3 quantum-dot films with efficient ligand passivation. *ACS Energy Lett.* **2019**, *4*, 2731−2738.

(29) Bi, C.; Wang, S.; Kershaw, S. V.; Zheng, K.; Pullerits, T.; Gaponenko, S.; Tian, J.; Rogach, A. L. Spontaneous Self-Assembly of Cesium Lead Halide Perovskite Nanoplatelets into Cuboid Crystals with High Intensity Blue Emission. *Adv. Sci.* **2019**, *6*, 1900462.

(30) Wang, Y.-K.; Ma, D.; Yuan, F.; Singh, K.; Pina, J. M.; Johnston, A.; Dong, Y.; Zhou, C.; Chen, B.; Sun, B. Chelating-agent-assisted control of CsPbBr 3 quantum well growth enables stable blue perovskite emitters. *Nat. Commun.* **2020**, *11*, 1−7.

https://doi.org/10.1021/acsnano.2c02795
ACS Nano XXXX, XXX, XXX−XXX

(31) Jin, X.; Zhang, X.; Fang, H.; Deng, W.; Xu, X.; Jie, J.; Zhang, X. Facile Assembly of High-Quality Organic-Inorganic Hybrid Perovskite Quantum Dot Thin Films for Bright Light-Emitting Diodes. *Adv. Funct. Mater.* **2018**, *28*, 1705189.
(32) Fu, P.; Shan, Q.; Shang, Y.; Song, J.; Zeng, H.; Ning, Z.; Gong, J. Perovskite nanocrystals: synthesis, properties and applications. *Sci. Bull.* **2017**, *62*, 369−380.
(33) Ashner, M. N.; Shulenberger, K. E.; Krieg, F.; Powers, E. R.; Kovalenko, M. V.; Bawendi, M. G.; Tisdale, W. A. Size-dependent biexciton spectrum in $CsPbBr_3$ perovskite nanocrystals. *ACS Energy Lett.* **2019**, *4*, 2639−2645.
(34) Castaneda, J. A.; Nagamine, G.; Yassitepe, E.; Bonato, L. G.; Voznyy, O.; Hoogland, S.; Nogueira, A. F.; Sargent, E. H.; Cruz, C. H. B.; Padilha, L. A. Efficient biexciton interaction in perovskite quantum dots under weak and strong confinement. *ACS Nano* **2016**, *10*, 8603−8609.
(35) Sun, S.; Yuan, D.; Xu, Y.; Wang, A.; Deng, Z. Ligand-mediated synthesis of shape-controlled cesium lead halide perovskite nanocrystals via reprecipitation process at room temperature. *ACS Nano* **2016**, *10*, 3648−3657.
(36) Zhu, F.; Men, L.; Guo, Y.; Zhu, Q.; Bhattacharjee, U.; Goodwin, P. M.; Petrich, J. W.; Smith, E. A.; Vela, J. Shape evolution and single particle luminescence of organometal halide perovskite nanocrystals. *ACS Nano* **2015**, *9*, 2948−2959.
(37) Duan, L.; Hu, L.; Guan, X.; Lin, C.; Wu, T. Quantum Dots for Photovoltaics: A Tale of Two Materials. *Adv. Energy Mater.* **2021**, *11*, 2100354.
(38) Rogach, A. L.; Eychmüller, A.; Hickey, S. G.; Kershaw, S. V. Infrared-emitting colloidal nanocrystals: synthesis, assembly, spectroscopy, and applications. *Small* **2007**, *3*, 536−557.
(39) Kalytchuk, S.; Gupta, S.; Zhovtiuk, O.; Vaneski, A.; Rogach, A. L. Semiconductor Nanocrystals as Luminescent Down-Shifting Layers To Enhance the Efficiency of Thin-Film CdTe/CdS and Crystalline Si Solar Cells. *J. Appl. Phys.* **2014**, *118*, 16393−16400.
(40) Wang, J.; Wang, N.; Jin, Y.; Si, J.; Tan, Z. K.; Du, H.; Cheng, L.; Dai, X.; Bai, S.; He, H. Interfacial control toward efficient and low-voltage perovskite light-emitting diodes. *Adv. Mater.* **2015**, *27*, 2311−2316.
(41) Meng, L.; Yao, E. P.; Hong, Z.; Chen, H.; Sun, P.; Yang, Z.; Li, G.; Yang, Y. Pure formamidinium-based perovskite light-emitting diodes with high efficiency and low driving voltage. *Adv. Mater.* **2017**, *29*, 1603826.
(42) Zhang, D.; Gu, L.; Zhang, Q.; Lin, Y.; Lien, D.-H.; Kam, M.; Poddar, S.; Garnett, E. C.; Javey, A.; Fan, Z. Increasing Photoluminescence Quantum Yield by Nanophotonic Design of Quantum-Confined Halide Perovskite Nanowire Arrays. *Nano Lett.* **2019**, *19*, 2850−2857.
(43) Aneesh, J.; Swarnkar, A.; Kumar Ravi, V.; Sharma, R.; Nag, A.; Adarsh, K. Ultrafast exciton dynamics in colloidal $CsPbBr_3$ perovskite nanocrystals: Biexciton effect and Auger recombination. *J. Phys. Chem. C* **2017**, *121*, 4734−4739.
(44) Yu, H.; Li, J.; Loomis, R. A.; Wang, L.-W.; Buhro, W. E. Two-versus three-dimensional quantum confinement in indium phosphide wires and dots. *Nat. Mater.* **2003**, *2*, 517−520.
(45) Ling, Y.; Yuan, Z.; Tian, Y.; Wang, X.; Wang, J. C.; Xin, Y.; Hanson, K.; Ma, B.; Gao, H. Bright light-emitting diodes based on organometal halide perovskite nanoplatelets. *Adv. Mater.* **2016**, *28*, 305−311.
(46) Ergen, O.; Ruebusch, D. J.; Fang, H.; Rathore, A. A.; Kapadia, R.; Fan, Z.; Takei, K.; Jamshidi, A.; Wu, M.; Javey, A. Shape-controlled synthesis of single-crystalline nanopillar arrays by template-assisted vapor- liquid- solid process. *J. Am. Chem. Soc.* **2010**, *132*, 13972−13974.
(47) Kresse, G.; Hafner, J. Ab initio molecular dynamics for liquid metals. *Phys. Rev. B* **1993**, *47*, 558.
(48) Kresse, G.; Hafner, J. Ab initio molecular-dynamics simulation of the liquid-metal-amorphous-semiconductor transition in germanium. *Phys. Rev. B* **1994**, *49*, 14251.
(49) Kresse, G.; Furthmüller, J. Efficient iterative schemes for ab initio total-energy calculations using a plane-wave basis set. *Phys. Rev. B* **1996**, *54*, 11169.
(50) Kresse, G.; Furthmüller, J. Efficiency of ab-initio total energy calculations for metals and semiconductors using a plane-wave basis set. *Comput. Mater. Sci.* **1996**, *6*, 15−50.
(51) Perdew, J. P.; Burke, K.; Ernzerhof, M. Generalized gradient approximation made simple. *Phys. Rev. Lett.* **1996**, *77*, 3865.
(52) Blöchl, P. E. Projector augmented-wave method. *Phys. Rev. B* **1994**, *50*, 17953.
(53) Monkhorst, H. J.; Pack, J. D. Special points for Brillouin-zone integrations. *Phys. Rev. B* **1976**, *13*, 5188.
(54) Grimme, S.; Antony, J.; Ehrlich, S.; Krieg, H. A consistent and accurate ab initio parametrization of density functional dispersion correction (DFT-D) for the 94 elements H-Pu. *J. Chem. Phys.* **2010**, *132*, 154104.
(55) Grimme, S.; Ehrlich, S.; Goerigk, L. Effect of the damping function in dispersion corrected density functional theory. *J. Comput. Chem.* **2011**, *32*, 1456−1465.

https://doi.org/10.1021/acsnano.2c02795
ACS Nano XXXX, XXX, XXX−XXX